






Visualizing coherent molecular rotation in a gaseous medium

Ilia Tutunnikov ¹, Emilien Prost,² Uri Steinitz ^{1,3}, Pierre Béjot,² Edouard Hertz ², Franck Billard,²
Olivier Faucher ^{2,*} and Ilya Sh. Averbukh ^{1,†}

¹*AMOS and Department of Chemical and Biological Physics, The Weizmann Institute of Science, Rehovot 7610001, Israel*

²*Laboratoire Interdisciplinaire CARNOT de Bourgogne Franche-Comté, UMR 6303 CNRS-Université de Bourgogne, BP 47870, 21078, Dijon, France*

³*Soreq Nuclear Research Centre, Yavne 8180000, Israel*



(Received 26 September 2021; accepted 3 November 2021; published 19 November 2021)

Inducing and controlling the ultrafast molecular rotational dynamics using shaped laser fields is essential in numerous applications. Several approaches exist that allow following the coherent molecular motion in real time, including Coulomb explosion-based techniques and recovering molecular orientation from the angular distribution of high harmonics. We theoretically consider a nonintrusive optical scheme for visualizing the rotational dynamics in an anisotropic molecular gas. The proposed method allows determining the instantaneous orientation of the principal optical axes of the gas. The method is based on probing the sample using ultrashort circularly polarized laser pulses and recording the transmission image through a vortex wave plate. We consider two example excitations: molecular alignment induced by an intense linearly polarized laser pulse and unidirectional molecular rotation induced by a polarization-shaped pulse. The proposed optical method is promising for visualizing the dynamics of complex symmetric- and asymmetric-top molecules.

DOI: [10.1103/PhysRevA.104.053113](https://doi.org/10.1103/PhysRevA.104.053113)

I. INTRODUCTION

Over the years, the scientific field of molecular alignment and orientation control generated an extensive set of tools, ranging from adiabatic and impulsive alignment by single linearly polarized laser pulses to orientation by combined laser fields with intricately tailored polarizations. Molecular alignment and unidirectional rotation (UDR) induced by laser fields have been reviewed in Refs. [1,2]. For broader reviews on molecular control using electromagnetic fields, the reader is referred to Refs. [3,4]. The problem of control comes hand in hand with the problem of visualization of the resulting dynamics.

In the early days, mainly Coulomb explosion technique was utilized for visualizing laser-induced one-dimensional molecular alignment. An intense time-delayed probe pulse ionized the molecules, and the yield of fragments ejecting along or against the polarization of the probe was detected [5,6]. This allowed recovering the degree of alignment, usually quantified by a single observable $\langle \cos^2 \theta \rangle$, where the angle brackets denote the average value. The angle θ is the angle between the molecular axis and the polarization direction of the aligning pulse. Later on, the approach evolved into a nowadays standard technique—velocity map imaging (VMI), allowing reconstruction of molecular angular distribution as a function of time [7]. For a recent example of the state of the art experiment using VMI, the reader is referred to Ref. [8] and the references therein. Another powerful tool

providing access to 3D information is the cold target recoil ion momentum spectroscopy (COLTRIMS) [9], where the electron and ion momenta are coincidentally detected. Methods based on imaging of charged fragments were successfully applied for imaging the dynamics of unidirectionally rotating molecules and orientation dynamics of asymmetric-top molecules [10–12]. While VMI and COLTRIMS provide a complete characterization of molecular rotation, this usually comes at a price of strict experimental conditions (rarefied gases and molecular beams), complex experimental setups, and long acquisition times.

Another class of methods relies on optical techniques which have many attractive practical advantages, e.g., a much-extended working range of pressures and temperatures [13]. So far, the optical detection schemes have been limited to one-dimensional measurements of the ensemble-averaged quantities, such as the degree of molecular orientation or alignment, quantified by $\langle \cos \theta \rangle$ [14,15] and $\langle \cos^2 \theta \rangle$ [15,16], respectively. Higher-order moments $\langle \cos^n \theta \rangle$, with $n > 2$, of the molecular angular distribution can be measured using harmonic generation [17,18]. Recently, angle-resolved high-order-harmonic spectroscopy was used for generating molecular “rotational movies” with the help of machine learning tools [19].

Here, we present a theoretical analysis of the recently demonstrated [20] purely optical approach allowing detecting the instantaneous orientation of the principal optical axes of a laser-excited molecular gas. The approach relies on ultrafast birefringence measurement using delayed femtosecond probe pulses. In the present paper, we concentrate on detailed discussion of the underlying physics behind the technique and reveal the relative roles of different mechanisms involved

*olivier.foucher@u-bourgogne.fr

†ilya.averbukh@weizmann.ac.il

in the formation of the imaging patterns. In particular, we consider the regime when the molecular medium is nonuniformly excited by an inhomogeneous pump beam (a rather typical experimental situation), which leads to the additional focusing of the probe beam and modifies the images. The analysis presented here is applicable to a wide range of experimentally accessible parameters, such as gas pressure, various widths of the pump and probe beams, and their intensities. The paper is organized as follows: Sec. II qualitatively describes the proposed imaging technique in the case of homogeneously excited molecular sample. In Sec. III, we present the numerical results obtained by solving the paraxial beam propagation equation. We use two example excitations: impulsive excitation by linearly polarized pulses resulting in a molecular dynamics that toggle between alignment and antialignment, and excitation by femtosecond polarization-twisted pulses which cause unidirectional rotation of the alignment axis. Sections IV and V describe the case of the inhomogeneous excitation and present the corresponding numerical results, respectively. Section VI concludes the paper.

II. QUALITATIVE DESCRIPTION—PLANAR WAVE CASE

We begin with a qualitative description of the proposed optical imaging approach. As an example, we consider the case of rigid linear molecules in the gas phase excited by a short *linearly polarized* in the XY plane pulse (pump pulse), propagating along the Z axis. Such an excitation results in a transient molecular alignment along the polarization axis of the pump pulse [1–4]. Due to quantum revivals [21,22], the alignment recurs periodically with a well-defined period. Each revival event consists of alignment and antialignment stages. During both stages, the molecular gas develops anisotropy—the refractive index for light polarized along the pump polarization axis differs from the refractive index for light polarized along the orthogonal direction. The two orthogonal optical principal axes in the XY plane, X' and Y' , have refractive indices $n_{X'}$ and $n_{Y'}$, respectively. In the case of linearly polarized pump pulse, we let X' to be the axis of the pump polarization. Here, the directions of X' and Y' axes are fixed, while the values of $n_{X'}$ and $n_{Y'}$ depend on the probe delay. We use a circularly polarized probe pulse, whose polarization can be decomposed onto the X' and Y' axes.

Since, generally $n_{X'} \neq n_{Y'}$, the two components of the probe light accumulate a relative phase as they propagate through the anisotropic medium. After passing the medium, the probe polarization becomes, therefore, elliptical. The orientation of the major axis of the ellipse depends on the orientation of the optical principal axes. For a homogeneous medium, the major axis of the polarization ellipse is at $\pm\pi/4$ to the optical axes. The sign depends on the sense of circular polarization and the stage of molecular dynamics (alignment or antialignment). One way to extract the information encoded in the polarization of the probe pulse is to use a polarization axis finder (PAF) [23,24], which renders a spatial intensity pattern having the same directionality as the polarization ellipse. In the present work, the PAF is composed of a vortex plate acting as a radial polarizer [25–29] and a linear polarizer. Recently, a similar PAF was successfully applied to imaging of coherent molecular rotors [20].

Qualitatively, given a circularly polarized light at the input plane, the electric field at an output plane can be determined with the help of Jones calculus [30]. Here, we adopt the same phase convention as in Ref. [30], namely, the phase of a monochromatic plane wave is defined as $kz - \omega t$, where k is the wave number, z is the position along the Z axis, ω is the angular frequency of light, and t is time. At the input plane, the Jones vector (expressed in the $X'Y'$ basis) of left-circular (from the point of view of the receiver) probe light propagating along the Z axis reads

$$\mathbf{u}_{X'Y'}(z_i) = \frac{1}{\sqrt{2}} \begin{pmatrix} 1 \\ i \end{pmatrix}, \quad (1)$$

where z_i denotes the position of the input plane. While propagating through the sample, the X' and Y' components of the probe light accumulate a relative phase δ , such that at the output plane z_o ,

$$\mathbf{u}_{X'Y'}(z_o) = \begin{pmatrix} 1/\sqrt{2} & 0 \\ 0 & e^{i\delta}/\sqrt{2} \end{pmatrix} \begin{pmatrix} 1 \\ i \end{pmatrix}, \quad (2)$$

where the sign of δ depends on the stage of molecular dynamics (alignment or antialignment). During the alignment stage, $n_{X'} > n_{Y'}$ making X' axis the slow axis, accordingly, the Y' component leads the X' component and, in the chosen phase convention, $\delta < 0$. Transforming back to the XY basis is achieved by $\mathbf{u}_{XY}(z = z_o) = R_Z(\chi)\mathbf{u}_{X'Y'}(z = z_o)$, where $R_Z(\chi)$ is the canonical rotation matrix about the Z axis, where χ is the angle between X' , the slow axis of the medium (here, the pump polarization axis), and X axes. This results in

$$\mathbf{u}_{XY}(z = z_o) = \frac{1}{\sqrt{2}} \begin{pmatrix} \cos \chi - ie^{i\delta} \sin \chi \\ ie^{i\delta} \cos \chi + \sin \chi \end{pmatrix}. \quad (3)$$

For $\delta < 0$ ($\delta > 0$), the Jones vector in Eq. (3) represents left (right) elliptical light. The major axis of the ellipse is oriented at angle $\pi/4 + \chi$ ($-\pi/4 + \chi$) relative to the positive X axis (or at angle $\pi/4$ ($-\pi/4$) relative to the principal X' axis).

For every point (with azimuth φ) on the PAF plane in the laboratory frame, the PAF in the XY basis has a specific Jones matrix representation,

$$\mathbf{M}_R = \begin{pmatrix} 1 & 0 \\ 0 & 0 \end{pmatrix} \begin{pmatrix} \cos \varphi & \sin \varphi \\ \sin \varphi & -\cos \varphi \end{pmatrix}, \quad (4)$$

where the right matrix represents a $m = 1$ vortex plate [25,26] (the first element of the PAF). The transformation induced by the vortex plate is equivalent to the transformation induced by a half-wave plate with a continuously varying angle of the fast axis, $\varphi/2$. The left matrix in Eq. (4) represents a linear polarizer oriented along the X axis (the second element of the PAF). The intensity as a function of the azimuthal angle at the image plane is given by

$$\begin{aligned} I(\varphi; \delta, \chi) &= |\mathbf{M}_R \mathbf{u}_{XY}(z = z_o)|^2 \\ &= \frac{1}{2} - \frac{1}{2} \sin(\delta) \sin[2(\varphi - \chi)]. \end{aligned} \quad (5)$$

The case of $\chi = 0$ corresponds to the molecular alignment along the X axis. Since the function in Eq. (5) depends on the difference $\varphi - \chi$, for $\chi \neq 0$, the images are simply rotated counterclockwise by angle χ . Figure 1 shows polar plots of

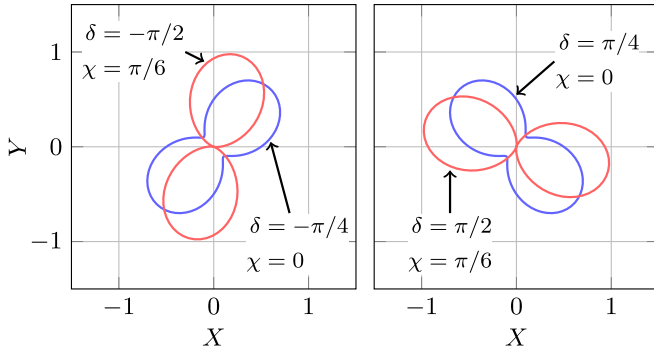


FIG. 1. Polar plots of the intensity in Eq. (5). Left—alignment stage, $\delta < 0$. Right—antialignment stage, $\delta > 0$.

the intensity in Eq. (5) for the alignment ($\delta < 0$) and antialignment ($\delta > 0$) stages, and for two angles $\chi = 0, \pi/6$. For $\delta = \mp\pi/2$, the outgoing probe becomes linearly polarized, such that the eight-shaped intensity pattern is most emphasized and it is oriented at an angle of $+\pi/4$ to the slow axis of the birefringent medium. When δ approaches zero, the pattern continuously transforms into a unit circle (isotropic case).

III. BEAM PROPAGATION SIMULATIONS— HOMOGENEOUS CASE

We consider a gas of rigid linear molecules excited by a nonresonant laser pulse (pump) propagating along the Z axis with linear or shaped polarization (restricted to the XY plane). Generally, laser excitation results in time-dependent anisotropy and inhomogeneity of the molecular gas.

The gaseous medium is probed by collinearly propagating time-delayed laser pulses (probe pulses). We neglect the difference between the group velocities of the pump and probe pulses (the Rayleigh length is short enough). Also, we assume that the probe pulse duration is much shorter than the time scale of molecular rotation, such that for a fixed probe delay, the probe pulse passes through effectively a time-independent medium. At the first stage, we assume that the molecular medium is homogeneous which is equivalent to assuming that the pump intensity is uniform across the XY plane and along the Z axis. This corresponds to the case when the waist radius and the Rayleigh range of the probe beam are smaller than those of the pump beam, such that the probe passes through a relatively homogeneous portion of the molecular sample. The propagation of the probe electric field \mathbf{E} through the anisotropic molecular gas is modeled using the wave equation

$$\nabla^2 \mathbf{E} - \frac{1}{c^2} \vec{\epsilon}_r(\tau) \frac{\partial^2 \mathbf{E}}{\partial t^2} = \mathbf{0}, \quad (6)$$

where c is the speed of light in vacuum, and $\vec{\epsilon}_r$ is the tensor of relative permittivity depending on the probe delay, τ . Derivation of the more general version of Eq. (6) is summarized in the Appendix A. We define the complex amplitude \mathbf{U} by $\mathbf{E}(x, y, z, t) = \mathbf{U}(x, y, z) \exp[i(k_0 z - \omega t)]$, neglecting the pulse nature of the probe, with ω and k_0 being the carrier frequency and the vacuum wave number of the probe light, respectively. Here, we use the same phase convention as in

Ref. [30] (see Sec. II). Applying the paraxial approximation to Eq. (6), we obtain the simplified equation describing the propagation of the complex amplitude $\mathbf{U} = (U_x, U_y)$ along the Z axis [see Eq. (A12)]:

$$\frac{\partial \mathbf{U}}{\partial z} = \frac{i}{2k_0} \nabla_T^2 \mathbf{U} + \frac{ik_0}{2} (\vec{\epsilon}_r - \mathbf{I}) \mathbf{U}. \quad (7)$$

Here, ∇_T^2 is the transverse Laplace operator, \mathbf{I} is the identity matrix. Under ordinary conditions, the relative permittivity of a molecular gas is simply related to the ensemble-averaged molecular polarizability tensor, $\langle \vec{\alpha} \rangle_{\text{lab}}$,

$$\vec{\epsilon}_r = \mathbf{I} + \frac{N}{\epsilon_0} \langle \vec{\alpha} \rangle_{\text{lab}}, \quad (8)$$

where N is the number density of the gas, and ϵ_0 is the vacuum permittivity. All the physical quantities in Eq. (8) are expressed in SI units. In terms of $\langle \vec{\alpha} \rangle_{\text{lab}}$, Eq. (7) reads

$$\frac{\partial \mathbf{U}}{\partial z} = \frac{i}{2k_0} \nabla_T^2 \mathbf{U} + i \frac{Nk_0}{2\epsilon_0} \langle \vec{\alpha} \rangle_{\text{lab}} \mathbf{U}. \quad (9)$$

Equation (9) is solved using standard numerical tools. Let us consider two examples of ensemble dynamics and their visualizations: (A) The transition from alignment to antialignment and (B) the rotation of the alignment axis.

A. Excitation by linearly polarized pump pulse

As the first example, we consider excitation by a short femtosecond linearly polarized (along X axis) pump pulse. Such an excitation induces molecular alignment [1,2]—a transient confinement of molecular axes along the line defined by the pump polarization. The relatively strong transient alignment appears immediately after the excitation and disappears shortly after that because of the molecular angular velocities dispersion. Due to quantum revivals [21,22], the transient alignment periodically recurs with a well-defined period (in case of linear molecules) $T_r = 1/(2Bc)$, where $B = \hbar/(4\pi I c)$ is the molecular rotational constant, and I is the moment of inertia (more directly, $T_r = 2\pi I/\hbar$). There are also fractional revivals emerging at multiples of $T_r/4$, $T_r/2$, etc. The degree of alignment is quantified by the expectation value $\langle \cos^2 \theta_X \rangle$ where θ_X is the angle between the laboratory X axis and the molecular axis. We consider the alignment of CO_2 molecules at initial rotational temperature $T = 300$ K. The moment of inertia (in atomic units, a.u.) of CO_2 molecule is $I = 280207$ a.u., and the molecular polarizabilities along and perpendicular to the molecular axis are $\alpha_{\parallel} = 30.1$ a.u. and $\alpha_{\perp} = 30.1$ a.u., respectively. Figure 2(a) shows the degree of alignment as a function of time (probe delay), following the excitation at $t = 0$.

For quantum mechanical simulations of the expectation values $\langle \cos^2 \theta_X \rangle$, the linear molecules were modeled as rigid polarizable rotors. The interaction energy with nonresonant pump pulse is given by $V = -\mathbf{E}_{\text{pump}} \cdot \mathbf{d}_{\text{ind}}/2 = -\mathbf{E}_{\text{pump}} \cdot (\vec{\alpha} \mathbf{E}_{\text{pump}})/2$, where $\mathbf{d}_{\text{ind}} = \vec{\alpha} \mathbf{E}_{\text{pump}}$ is the induced dipole, and \mathbf{E}_{pump} is the pump electric field. Our numerical scheme for simulating the laser driven dynamics of complex rigid molecules is described in Ref. [31]. In the present case, the scheme is specialized to the case of linear molecules.

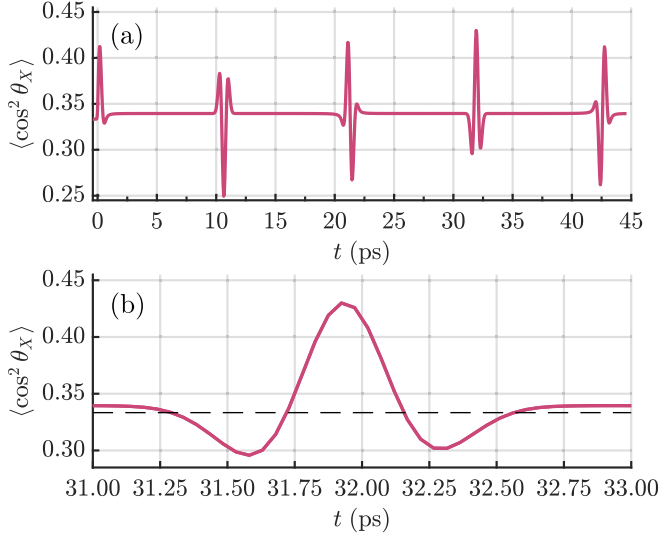


FIG. 2. (a) Degree of alignment, quantified by $\langle \cos^2 \theta_X \rangle$. Pump peak intensity $I_0 = 20 \text{ TW/cm}^2$. The full width at half maximum of the pulse is 100 fs and the initial molecular rotational temperature is $T = 300 \text{ K}$. (b) Enlarged portion of panel (a). The dashed line denotes the degree of alignment in undisturbed gas, $1/3$, which is considered the threshold between alignment to anti-alignment (alignment values lower than $1/3$).

The alignment factor shown in Fig. 2 is used to calculate the components of ensemble averaged polarizability tensor in the laboratory frame [13], $\langle \vec{\alpha} \rangle_{\text{lab}}$,

$$\langle \vec{\alpha} \rangle_{\text{lab},XX}(\tau) = \alpha_{\perp} + \Delta\alpha \langle \cos^2 \theta_X \rangle(\tau), \quad (10)$$

$$\langle \vec{\alpha} \rangle_{\text{lab},YY}(\tau) = \alpha_{\perp} + \frac{\Delta\alpha}{2} [1 - \langle \cos^2 \theta_X \rangle(\tau)], \quad (11)$$

where $\Delta\alpha = \alpha_{\parallel} - \alpha_{\perp}$. In the considered case, the pump pulse is polarized along the X axis, therefore the off-diagonal elements of $\langle \vec{\alpha} \rangle_{\text{lab}}$ vanish,

$$\langle \vec{\alpha} \rangle_{\text{lab},XY} = \langle \vec{\alpha} \rangle_{\text{lab},YX} = 0. \quad (12)$$

The polarizability tensor components in Eqs. (10) and (11) are used in Eq. (9) to simulate the probe propagation through the molecular gas. As described in Sec. II, the probe light is initially circularly polarized. The parameters we used are a Gaussian beam with a wavelength $\lambda_{\text{probe}} = 400 \text{ nm}$, waist $\omega_{0,\text{probe}} = 20 \mu\text{m}$, and Rayleigh length $z_{R,\text{probe}} = 3.14 \text{ mm}$.

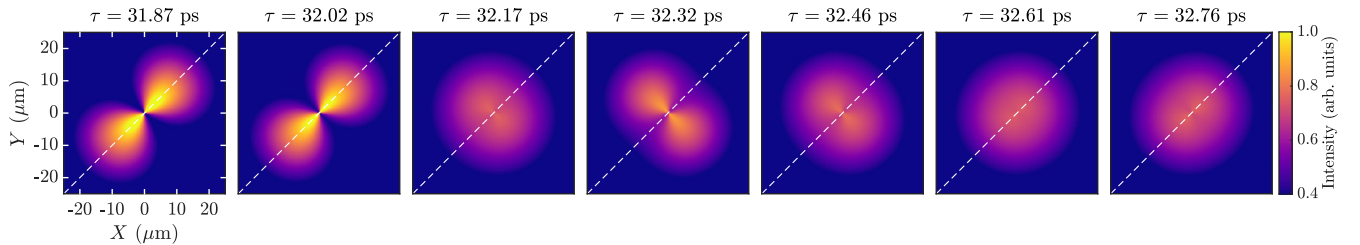


FIG. 3. Intensity of the probe beam after the PAF (see text) as a function of the probe delay, τ , during the fractional revival at $t \approx 3T_r/4$. Here, the molecules are excited by a linearly polarized along X axis pump pulse. The probe pulse at the input plane is given by Eq. (15). Probe light propagates through $\approx 7 \text{ mm}$ of the molecular gas. The shown images are taken after an additional 1 mm propagation through an undisturbed gas.

A typical length (along the Z axis) of the effectively excited molecular medium is about 7 mm. Using Eq. (9), we propagate the probe beam starting at the input plane $z = z_i = -3.5 \text{ mm}$ up to the output plane $z = z_o = 3.5 \text{ mm}$. The initial beam radius is

$$w(z_i) = w_{0,\text{probe}} \sqrt{1 + \left(\frac{z_i}{z_{R,\text{probe}}} \right)^2} = 30 \mu\text{m}. \quad (13)$$

The radius of curvature of the Gaussian beam at the input plane is

$$R(z_i) = z_i \left[1 + \left(\frac{z_{R,\text{probe}}}{z_i} \right)^2 \right] = -6.32 \text{ mm}, \quad (14)$$

while the initial complex amplitude is

$$U_X(x, y, z_i) = \exp \left(-\frac{x^2 + y^2}{w^2(z_i)} + ik_0 \frac{x^2 + y^2}{2R(z_i)} \right),$$

$$U_Y(x, y, z_i) = iU_X, \quad (15)$$

where $w(z_i)$ and $R(z_i)$ are defined in Eqs. (13) and (14), respectively. The complex amplitude describing the probe beam at z_o is found by numerically solving the equation in Eq. (9) with the initial condition in Eq. (15). Here, X and Y components of the complex amplitude vector are decoupled, because the off-diagonal elements of the polarizability in the laboratory frame vanish [see Eq. (12)]. Exiting the gas sample, the probe passes through the PAF (see Sec. II).

Figure 3 shows a series of intensity maps of the probe beam after the PAF at several delays during the fractional revival at $t = 3T_r/4$ (see Fig. 2), which is characterized by a transition from molecular alignment to anti-alignment. Here, the number density of the gas is set to $N = 0.02504 \times 10^{26} \text{ m}^{-3}$ [see Eq. (9)], corresponding to a pressure of approximately 0.1 atm. During the alignment stage, $31.75 \leq t \leq 32.12$ [see Fig. 2(b)], the intensity pattern is at angle $+\pi/4$ relative to the X axis (axis of pump polarization, principal optical axis X'). During the anti-alignment stage, $31.25 \leq t \leq 31.75$ and $32.12 \leq t \leq 32.60$ [see Fig. 2(b)], the intensity pattern is at angle $-\pi/4$ relative to the X axis. These results are in line with the qualitative discussion in Sec. II. Indeed, during the molecular alignment stage, the refractive index for the probe light component polarized along the X axis is higher, resulting in an accumulation of a relative phase between X and Y polarization components. In other words, the input circular polarization transforms into elliptical polarization with semimajor axis of the ellipse being oriented at angle $\pi/4$

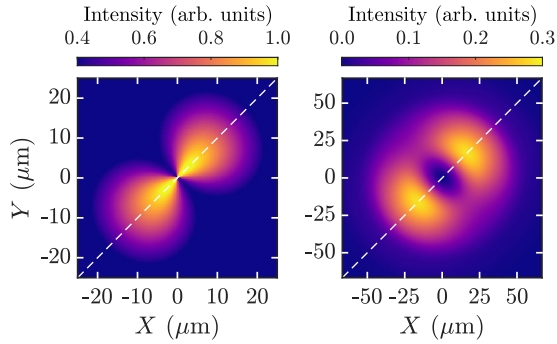


FIG. 4. Comparison between the images obtained after the PAF. Left—assuming the vortex plate is attached to the linear polarizer. Right—when the vortex plate and the linear polarizer are spaced apart by 2 mm. Here, the probe delay is $\tau = 32.02$ ps (see Fig. 3), and the vortex plate is at a distance of 1 mm away from the medium.

relative to the X axis (the slow axis of the medium). During the antialignment stage, X polarization component leads, and the semimajor axis of the ellipse is oriented at angle $-\pi/4$ to the X axis (fast axis of the medium). The PAF allows visualizing the orientation of the semimajor axis by producing an anisotropic intensity pattern with the same orientation as the semimajor axis, thus allowing detecting the orientation of principal optical axes of the medium. Notice, between the revivals, there is a small persistent alignment which is reflected in weak anisotropy visible in the last panel in Fig. 3.

Let us note that in practice, the vortex plate and linear polarizer (forming together the PAF) are spaced apart, and the vortex plate applies an angle-dependent phase mask [see Eq. (4)] to the incident beam. Therefore, while propagating between the vortex plate to the polarizer, the incident Gaussian probe beam disperses and evolves into a doughnut-like shape, such that the experimental images look more like shown in the right panel of Fig. 4 (also, see the experimental results in Ref. [20]). Moreover, in experiments, for practical reasons, the image plane is located much farther from the excitation volume (far-field measurement). The images shown here do not represent the actual scale expected in the experiments. The scale depends on the optical distance and the lenses system between the gas cell and the imaging device.

B. Excitation by polarization-twisted pump pulse

As an additional example, we consider the excitation by a polarization shaped pulse with twisted polarization [32]. A polarization-twisted pulse is modeled as a pair of two in-phase overlapping orthogonally polarized laser pulses with a delay τ_p between them. The corresponding electric field reads

$$\mathbf{E}_{\text{pump}}(t) = E_0[f(t)\mathbf{e}_X + f(t - \tau_p)\mathbf{e}_Y] \cos(\omega t), \quad (16)$$

where E_0 is the peak amplitude, \mathbf{e}_X and \mathbf{e}_Y are the unit vectors along the laboratory X and Y axes. The envelope $f(t)$ of each constituent linearly polarized pulse is Gaussian. Figure 5 shows an illustration of the polarization vector twisting from the X axis to the Y axis.

In contrast to the excitation by a linearly polarized pump pulse, here, the Z projection of molecular angular momentum is not conserved as the twisting polarization induces molec-

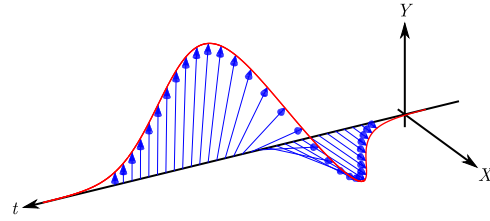


FIG. 5. Illustration of the polarization twisting; see Eq. (16).

ular unidirectional rotation (UDR) about the Z axis [33]. In this case, the description of molecular rotations required two dynamical degrees of freedom. It is convenient to use the two standard spherical coordinate system angles: polar angle θ between the Z axis and the molecular axis, and azimuthal angle ϕ between the projection of the molecular axis on the XY plane and the positive X axis. In the case of UDR the polarizability tensor, $\langle \vec{\alpha} \rangle_{\text{lab}}$ is no longer diagonal, because the principal optical axes (X' and Y') do not generally overlap with X and Y axes, and their orientation changes with time. The off-diagonal elements of $\langle \vec{\alpha} \rangle_{\text{lab}}$, reflecting the unidirectional rotation of the molecular axis [32,34], read

$$\langle \vec{\alpha} \rangle_{\text{lab},XY} = \langle \vec{\alpha} \rangle_{\text{lab},YX} = \frac{\Delta\alpha}{2} \langle \sin(2\phi) \sin^2(\theta) \rangle. \quad (17)$$

Explicit expressions for all the elements of $\langle \vec{\alpha} \rangle_{\text{lab}}$ parameterized by θ and ϕ are given in Appendix B, see Eqs. (B5)–(B8). Figure 6(a) shows the time dependence of the off diagonal element (divided by $\Delta\alpha$) in Eq. (17). Figure 6(b) shows the

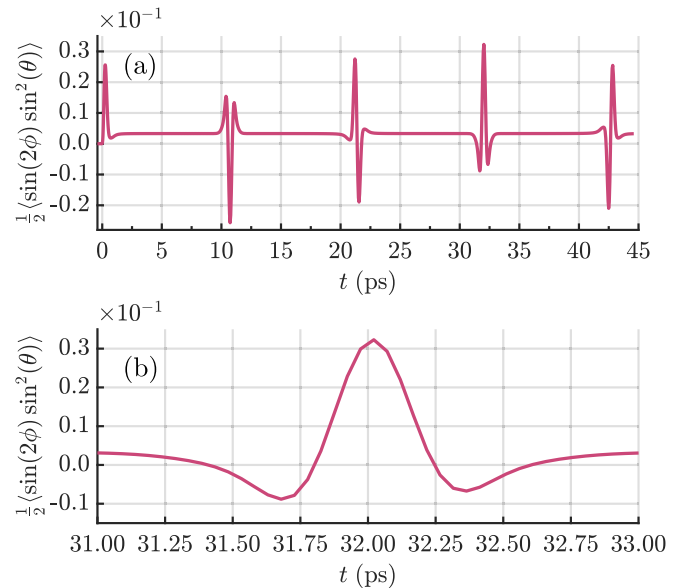


FIG. 6. (a) The curve is proportional to the off-diagonal element of the polarizability tensor; see Eq. (17). Parameters of the polarization twisted pump pulse: peak intensity $I_0 = 20$ TW/cm², full width at half maximum of each constituent linearly polarized pulse is 100 fs, the delay between the pulses is $\tau_p = 150$ fs. Initial molecular rotational temperature is $T = 300$ K. (b) Enlarged portion of panel (a).

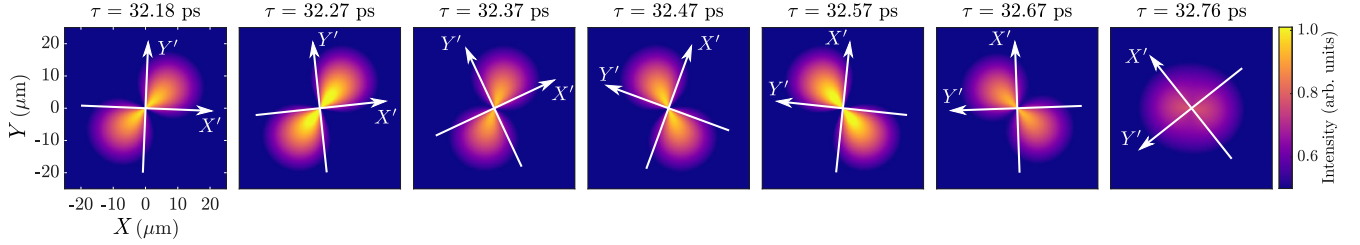


FIG. 7. Intensity of the probe beam after the PAF as a function of the probe delay, τ , during the fractional revival at $t \approx 3T_r/4$. Here, the molecules are excited by a polarization twisted pulse [see Eq. (16)]. The delay τ is measured from the center of the first linearly polarized (along X) pulse forming the polarization twisted pulse. The rest is the same as in Fig. 3.

magnified portion during the fractional quantum revival at $t \approx 3T_r/4$.

Figure 7 shows a series of intensity images of the probe beam after the PAF at several delays during the fractional revival at $t \approx 3T_r/4$. In addition to the anisotropy (like in the case of excitation by a linearly polarized pulse) the principal optical axes, X' and Y' , also rotate in the XY plane. This rotation is the manifestation of molecular UDR.

IV. QUALITATIVE DESCRIPTION— INHOMOGENEOUS CASE

So far, we considered the case of uniformly excited molecular medium, and only the birefringence effect has been taken into account. Generally, however, when the probe beam waist is comparable with the waist of the pump pulse, the inhomogeneity needs to be taken into account. The aforementioned inhomogeneity stems from the fact that the pump intensity decreases away from the optical axis, resulting in the variation of the molecular alignment across the transverse plane. In the same manner, on the Z axis, the pump intensity (and its induced molecular effect) reduces with the distance from the focal plane.

Once again, for simplicity, we consider the case of excitation by a linearly polarized pump pulse, polarized at an angle χ to the X axis. The transverse molecular alignment inhomogeneity acts as an effective lens, as it manifests in a graded refractive index. Generally, the two orthogonal probe components, X' and Y' , focus differently. During the alignment stage, the X' components is focused, while the Y' component is defocused and vice versa during the antialignment stage [35]. Qualitatively, the focusing effect can be described by introducing the attenuation parameter $0 \leq a \leq 1$, such that [compare to Eq. (2)]

$$\mathbf{u}_{X'Y'}(z_0) = \begin{pmatrix} \sqrt{1-a^2} & 0 \\ 0 & ae^{i\delta} \end{pmatrix} \begin{pmatrix} 1 \\ i \end{pmatrix}. \quad (18)$$

For $a = 1/\sqrt{2}$, Eq. (18) reduces to Eq. (2). Notice, the definition of parameter a implies that the beam's energy at a fixed radial distance is conserved. In reality, however, the *total* energy is conserved. Therefore, a should be treated as an effective parameter accounting for the unequal intensities of the two polarization components of the probe beam at a particular radial distance from the optical axis and at particular z_0 . The

intensity at the output plane reads [compare with Eq. (5)]

$$I(\varphi; \delta, \chi, a) = \frac{1}{2} - a\sqrt{1-a^2} \sin(\delta) \sin[2(\varphi - \chi)] + \left(\frac{1}{2} - a^2\right) \cos[2(\varphi - \chi)]. \quad (19)$$

Figure 8 shows polar plots of the intensity in Eq. (19). During the alignment stage ($\delta < 0$, $a < 1/\sqrt{2}$), the probe component polarized along the X' axis is focused, while the Y' components is defocused. The eight-shaped intensity pattern is effectively pushed closer to the X' axis. During the antialignment stage ($\delta > 0$, $a > 1/\sqrt{2}$), the probe component polarized along the Y' axis is focused, while the X' components is defocused. The eight-shaped intensity pattern is effectively pushed closer to the Y' axis.

The angle γ (in radians) between the X' (Y') axis for the case $\delta < 0$, $a < 1/\sqrt{2}$ ($\delta > 0$, $a > 1/\sqrt{2}$) and the long axis of the eight-shaped intensity pattern (see Fig. 8) can be found from $\partial_\varphi I(\varphi; \delta, \chi, a)|_\gamma = 0$. Explicitly,

$$\gamma = \frac{1}{2} \arctan \left(\frac{2a \sin(\delta) \sqrt{1-a^2}}{2a^2 - 1} \right), \quad (20)$$

Generally, angle γ also depends on the radial distance from the optical axis and the position along the optical axis. The reason is that the ratio of intensities of the two polarization components changes with radial and longitudinal positions.

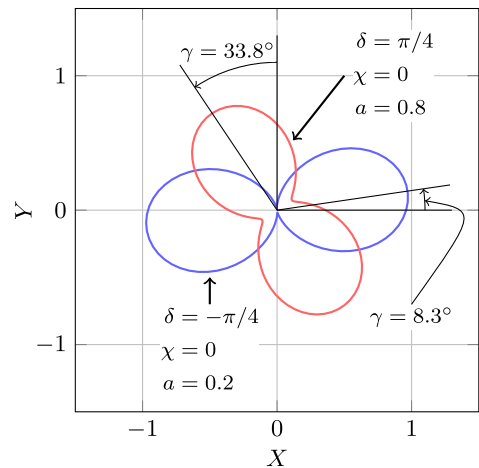


FIG. 8. Polar plots of the intensity in Eq. (19) calculated for alignment (blue) and antialignment (red) induced by a pump polarized along the X axis. The angle γ is given by Eq. (20).

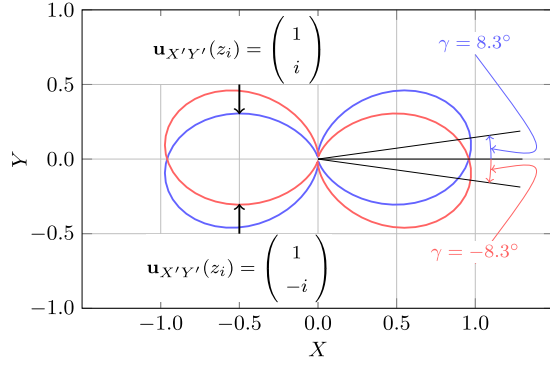


FIG. 9. Polar plots for left- (blue) and right-handed (red) probes [see Eqs. (19) and (21)]. The angle γ for the case of left circular probe is given by Eq. (20). The other parameters are $\delta = -\pi/4$, $\chi = 0$, and $a = 0.2$.

In the case of negligible focusing, $a \rightarrow 1/\sqrt{2}$, $\gamma \rightarrow \pi/4$ [see Eq. (5) and Fig. 1].

At this point, we would like to draw the reader's attention to that in the case of nonnegligible focusing, the orientation of the optical principal axes is ambiguous. Indeed, consider, e.g., the blue curve in Fig. 8. What is the reason behind $\gamma \neq \pm\pi/4$? There are two possible reasons (or a combination thereof): (i) the principal optical axes are rotated $\chi \neq 0$, while $\gamma = \pm\pi/4$, (ii) X' and Y' axes coincide with X and Y axes ($\chi = 0$), but there is a nonnegligible focusing, $\gamma \neq \pm\pi/4$. One way to resolve the ambiguity is to perform an additional measurement using circular probe light of opposite handedness. It can be shown that for the right circular probe, the intensity after the PAF reads [compare with Eq. (19)]

$$I(\varphi; \delta, \chi, a) = \frac{1}{2} + a\sqrt{1-a^2} \sin(\delta) \sin[2(\varphi - \chi)] + \left(\frac{1}{2} - a^2\right) \cos[2(\varphi - \chi)]. \quad (21)$$

Notice the plus sign in front of the second terms compared to Eq. (19). Moreover, angle γ [see Eq. (20)] has an opposite sign for the opposite circular polarizations. Figure 9 compares the intensities obtained for the probes of opposite handedness in the case of nonnegligible focusing.

The pictures obtained from the two measurements together, in principle, enable to determine the orientations of the optical principal axes (and to assess the focusing strength). As shown in Fig. 9, the principal axis bisects the angle between the long axis of the two intensity patterns.

TABLE I. Summary of the beams' parameters. Here λ , w_0 , z_R are vacuum wavelength, waist radius and Rayleigh range.

Beam	λ (nm)	w_0 (μm)	z_R (mm)
Pump	800	30	3.53
Probe	400	20	3.14

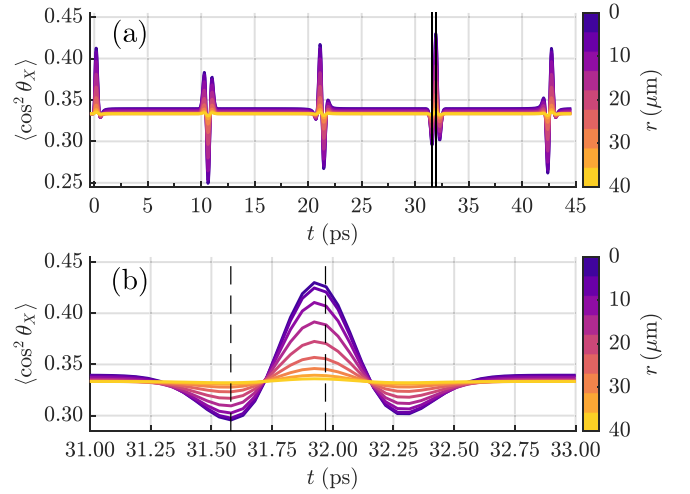


FIG. 10. (a) Degree of alignment at various transverse distances r from the optical axis. The pump peak intensity is $I(r=0) = 20 \text{ TW/cm}^2$ and the pump pulse duration at full width at half maximum (FWHM) is 100 fs. Initial molecular rotational temperature is $T = 300 \text{ K}$. (b) Enlarged portion of panel (a). Black vertical lines denote the delays shown in Fig. 11.

V. BEAM PROPAGATION SIMULATIONS—INHOMOGENEOUS CASE

In the case of nonnegligible inhomogeneity, the permittivity of the medium becomes coordinate-dependent and the wave equation reads [compare with Eq. (6)]

$$\nabla^2 \mathbf{E} - \frac{1}{c^2} \vec{\epsilon}_r(x, y, z; \tau) \frac{\partial^2 \mathbf{E}}{\partial t^2} = 0. \quad (22)$$

Defining the complex amplitude \mathbf{U} , and using the paraxial approximation, we arrive at the same equation as Eq. (9), but with coordinate dependent polarizability tensor $(\vec{\alpha})_{\text{lab}}$. The derivation is summarized in Appendix A. Again, we consider the dynamics of alignment to antialignment transition and the rotation of the alignment axis.

A. Excitation by linearly polarized pump pulse

Considering first the excitation by a linearly polarized along the X axis pump pulse. Similar to Sec. III A, the polarizability $(\vec{\alpha})_{\text{lab}}$ is diagonal, and its components are given by Eqs. (10) and (11). However, in contrast to Sec. III A, the degree of alignment now also depends on the coordinates

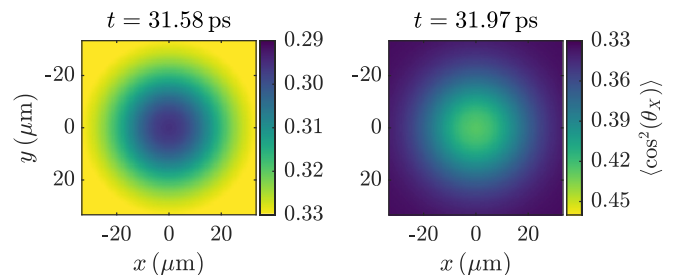


FIG. 11. The spatial variation of the degree of alignment at two times denoted by vertical lines in Fig. 10.

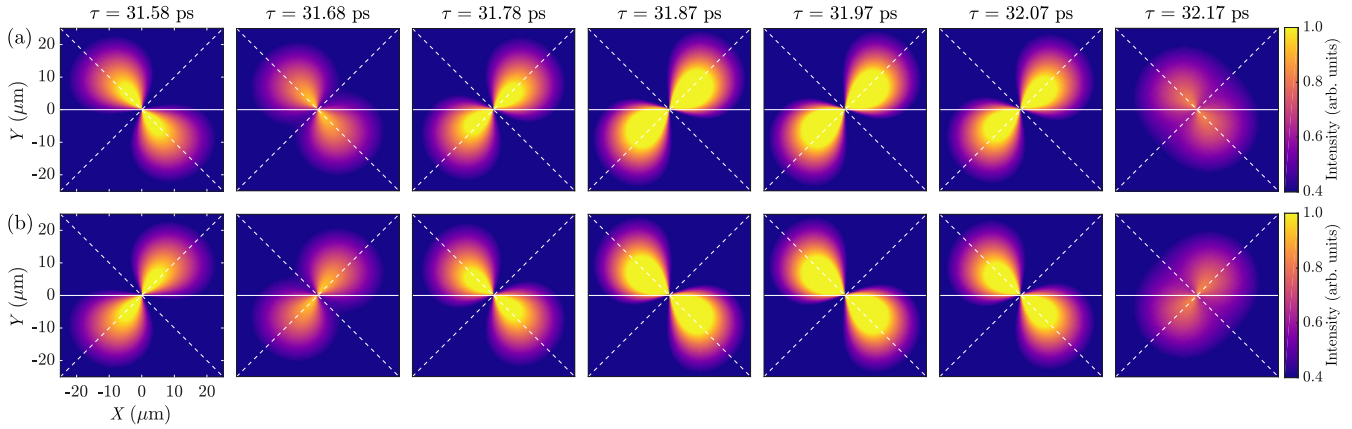


FIG. 12. Intensity of the probe beam after the PAF as a function of the delay, τ , during the fractional revival at $t \approx 3T_r/4$. Here, the molecules are excited by a linearly polarized along X -axis pump pulse. Probe light propagates through ≈ 7 mm of the molecular gas. The beams' parameters are defined in Table I. The shown images are taken after an additional propagation of 1 mm through an undisturbed gas. (a) Left circular probe. (b) Right circular probe.

$\langle \cos^2 \theta_X \rangle = \langle \cos^2 \theta_X \rangle(x, y, z; \tau)$. Following Ref. [20], we assume that the probe light is derived from the pump light by frequency doubling, and both have Gaussian profiles. Table I summarize the beams parameters used. To simplify matters, we neglect the inhomogeneity along the propagation direction (Z axis), such that $\langle \cos^2 \theta_X \rangle = \langle \cos^2 \theta_X \rangle(x, y; \tau)$.

Figure 10 shows several curves of time-dependent alignment factors at various transverse distances, r from the optical axis for the case of CO_2 molecules. Since the intensity of the pump decreases with the distance from the optical axis, the overall degree of alignment decreases as well. Here, the initial rotational temperature is $T = 300$ K.

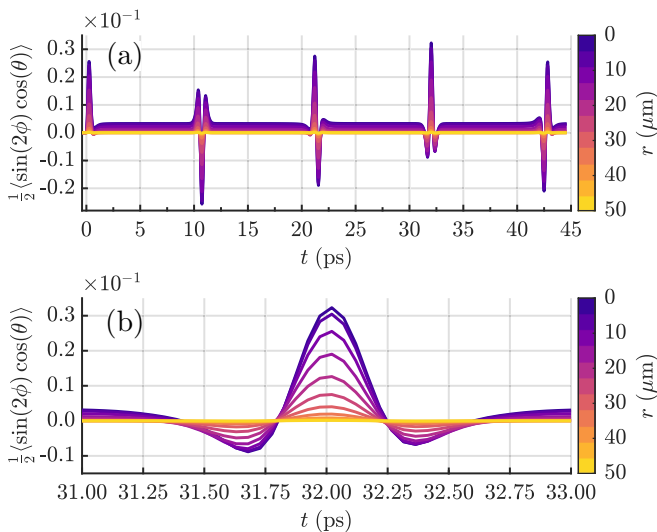


FIG. 13. The curves are proportional to the off-diagonal element of the polarizability tensor at various transverse distances, r from the optical axis. Parameters of the polarization-twisted pump pulse: peak intensity $I(r = 0) = 20$ TW/cm² and the width (FWHM) of each constituent linearly polarized pulse is 100 fs, the delay between the pulses is $\tau_p = 150$ fs. Initial molecular rotational temperature is $T = 300$ K. (b) Enlarged portion of panel (a).

Figure 11 shows the spatial dependence of the degree of alignment in the XY plane. The left panel ($t = 31.58$ ps) corresponds to the anti-alignment stage, while the right panel ($t = 31.97$ ps) corresponds to the alignment stage. These two moments are denoted by the vertical lines in Fig. 10. Considering Eqs. (10) and (11) and the wave equation in Eq. (9), the X' and Y' components (here, same as X and Y) of the probe pulse pass through effective lenses with curvatures $[(\cos^2 \theta_X)(x, y) - 1/3]$ and $[(\cos^2 \theta_Y)(x, y) - 1/3]$ [with $\langle \cos^2 \theta_Y \rangle(x, y) = -2 \langle \cos^2 \theta_X \rangle(x, y)$], respectively (see Fig. 11). Accordingly, the X' component is focused, while the Y' component is defocused, and vice versa during the anti-alignment stage.

Figure 12 shows a series of intensity images of the probe beam after the PAF at several delays during the fractional revival at $t = 3T_r/4$ (see Fig. 10). Here, the number density of the gas is set to $N = 0.1252 \times 10^{26} \text{ m}^{-3}$ [see Eq. (9)], corresponding to pressure of approximately 0.5 atm. Figure 12(a) shows the intensities obtained using a left circular probe [see Eq. (15)], while Fig. 12(b) shows the results obtained using a right circular probe ($U_Y = -iU_X$). In both cases, due to the focusing effect, the long axes of the intensity patterns slightly deviate from the diagonals. As mentioned previously (see Sec. IV), the degree of deviation of the long axis of the eight-shaped intensity from $\pm 45^\circ$, generally, depends on the radial distance r and the PAF and output plane's position. Here, the radial dependence is barely noticeable, while the change with the longitudinal distance, z is visible (not shown). The deviation is in the opposite directions for the opposite circular polarizations. This allows determining the orientations of the principal optical axes unambiguously. It is important to emphasize that due to the symmetry of excitation, the orientations of the optical principal axes, X' and Y' , are independent of the distance from the optical axis.

B. Excitation by polarization-twisted pump pulse

Next, we consider the excitation by the polarization-twisted pulse [see Eq. (16) and Fig. 5]. Similar to Sec. III B, the polarization-twisted pulse induces molecular UDR, which

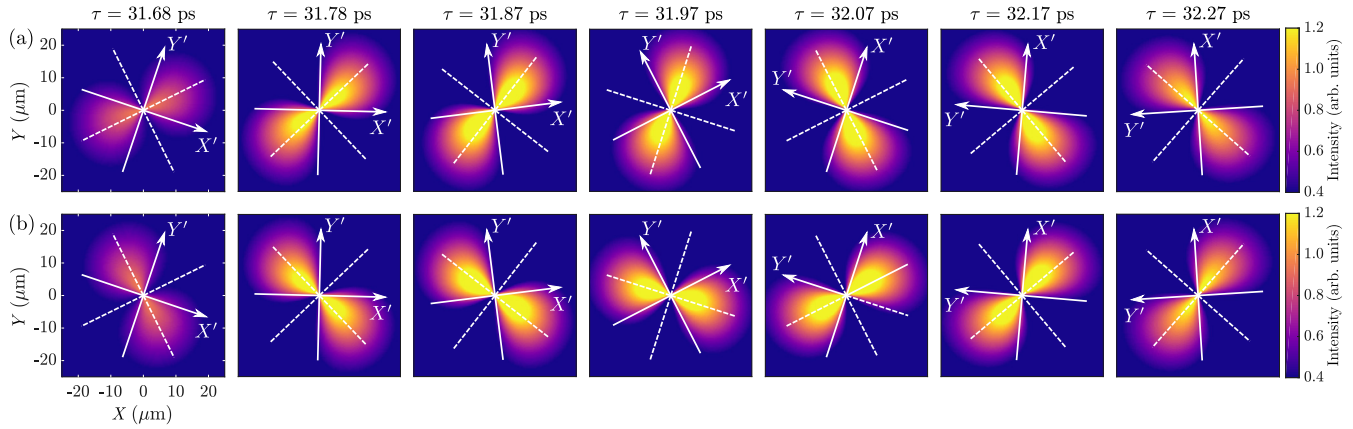


FIG. 14. Intensity patterns after the PAF as a function of the probe delay, τ , during the fractional revival at $t \approx 3T_r/4$. Here, the molecules are excited by a polarization-twisted pulse [see Eq. (16)]. The delay is measured from the peak of the first linearly polarized pulse. Rest of the parameters are similar to Fig. 12. (a) Left circular probe. (b) Right circular probe.

recurs during the fractional revivals. Figure 13 shows the off-diagonal element of the polarizability [divided by $\Delta\alpha$, see Eq. (17)] for various transverse distances, r from the optical axis. The existence of nonzero time-dependent (probe delay dependent) off-diagonal elements of the polarizability implies that the orientation of the optical principal axes changes with time.

There is an important difference between the excitation by polarization-twisted pulse having inhomogeneous intensity profile and the excitation by polarization-twisted pulse with homogeneous intensity considered in Sec. III B. In the case of twisted pulse the orientation of the optical axes generally depends on the radial distance from the optical axis. The physical reason for this is that the efficiency of the induced molecular UDR depends on the parameters of the polarization-twisted pulses.

Figure 14 shows a series of intensity images like in Fig. 12, but for the case of excitation by polarization twisted pulse. The white arrows denote the principal optical axes. As mentioned above, the orientation of X' and Y' axes depends on the radial distance; however, here the effect remains marginal within the waist of the pump pulse ($w_{0,\text{pump}} = 30 \mu\text{m}$). The shown principal axes were found by diagonalizing $\langle \vec{\alpha} \rangle_{\text{lab}}$ at $r = 20 \mu\text{m}$.

Thanks to the weak r dependence, the long axes of the intensity patterns deviate from the chosen principal axes in approximately the opposite sense for the probes of opposite circular polarization.

VI. CONCLUSIONS

We theoretically analyzed the optical imaging scheme introduced in Ref. [20], allowing direct visualization of the instantaneous orientation of the optical principal axes in a gas of laser-excited coherently rotating molecules. Time-delayed circularly polarized probe pulses are used to investigate the time-dependent optical birefringence of the molecular medium. A polarization axis finder (PAF) is used to visualize the polarization of the probe pulse, which contains the information on the optical principal axes. While in this work, we considered two examples of molecular excitation by short

pulses, the same approach applies to the visualization of other complex molecular states created by means of tailored laser pulses, e.g., molecular super rotors [36].

The proposed imaging scheme is directly applicable to symmetric-top molecules. Future works may extend the method to asymmetric-top molecules, which generally have three distinct polarizability axes, but additional experimental and theoretical studies are required. A purely optical approach may be promising for imaging alignment and unidirectional rotation of complex molecules (including chiral ones). Visualization of the dynamics of such molecules in traditional methods, e.g., Coulomb explosion-based methods, is challenging due to the multitude of possible fragments and ionization channels. The optical measurement of alignment dynamics may stimulate the development of imaging schemes suitable for tracing out intricate molecular *orientation* dynamics.

ACKNOWLEDGMENTS

This work was supported by the Israel Science Foundation (Grant No. 746/15), the CNRS, the ERDF Operational Programme-Burgundy, the EIPHI Graduate School (Contract No. ANR-17-EURE-0002), and the Associate (CNRS&Weizmann) International ImagiNano Laboratory. I.A. acknowledges support as the Patricia Elman Bildner Professorial Chair. This research was made possible in part by the historic generosity of the Harold Perlman Family.

APPENDIX A: WAVE EQUATION

Here, we derive the wave equation describing the propagation of a Gaussian beam in a nonmagnetic, inhomogeneous, and time independent molecular gas. Maxwell's equations (SI units) in matter which is free of currents and charges are

$$\nabla \times \mathbf{H} = \frac{\partial \mathbf{D}}{\partial t}, \quad (\text{A1})$$

$$\nabla \times \mathbf{E} = -\frac{\partial \mathbf{B}}{\partial t}, \quad (\text{A2})$$

$$\nabla \cdot \mathbf{D} = 0, \quad (\text{A3})$$

$$\nabla \cdot \mathbf{B} = 0, \quad (\text{A4})$$

where \mathbf{E} and \mathbf{B} are the electric and magnetic field vectors, \mathbf{H} and \mathbf{D} are the magnetizing and displacement field vectors. In addition to the Maxwell's equation, we use the constitutive relations

$$\mathbf{D} = \varepsilon_0 \vec{\varepsilon}_r \mathbf{E} \quad \mathbf{B} = \mu_0 \vec{\mu}_r \mathbf{H}, \quad (\text{A5})$$

where ε_0 and $\vec{\varepsilon}_r$ are the vacuum and relative permittivities, respectively, μ_0 and $\vec{\mu}_r$ are the vacuum and relative permeabilities, respectively. We assume a nonmagnetic medium, $\vec{\mu}_r = 1$. Relative permittivity $\vec{\varepsilon}_r$ is position dependent, but time independent tensor. Applying the curl operator to the Eq. (A2) results in

$$\begin{aligned} \nabla \times \left[(\nabla \times \mathbf{E}) + \frac{\partial \mathbf{B}}{\partial t} \right] &= \nabla \times (\nabla \times \mathbf{E}) \\ + \mu_0 \frac{\partial}{\partial t} (\nabla \times \mathbf{H}) &= 0, \end{aligned} \quad (\text{A6})$$

where the time derivative and curl operators were interchanged. Substituting $\nabla \times \mathbf{H} = \partial_t \mathbf{D}$ [see Eq. (A1)], we get

$$\begin{aligned} \nabla \times (\nabla \times \mathbf{E}) + \mu_0 \frac{\partial^2 \mathbf{D}}{\partial t^2} &= \nabla \times (\nabla \times \mathbf{E}) \\ + \mu_0 \varepsilon_0 \vec{\varepsilon}_r \frac{\partial^2 \mathbf{E}}{\partial t^2} &= 0. \end{aligned} \quad (\text{A7})$$

Using the vector identity $\nabla \times (\nabla \times \mathbf{A}) = \nabla(\nabla \cdot \mathbf{A}) - \nabla^2 \mathbf{A}$, we can simplify Eq. (A7)

$$\nabla^2 \mathbf{E} - \mu_0 \varepsilon_0 \vec{\varepsilon}_r \frac{\partial^2 \mathbf{E}}{\partial t^2} = \nabla(\nabla \cdot \mathbf{E}). \quad (\text{A8})$$

For our applications, we would like to simplify Eq. (A8) by neglecting $\nabla(\nabla \cdot \mathbf{E})$. To estimate the relative size of $\nabla(\nabla \cdot \mathbf{E})$, we assume that $\vec{\varepsilon}_r = \varepsilon_r(x, y, z)$ is a scalar and use Eq. (A3), $\nabla \cdot \mathbf{D} = \varepsilon_0 \nabla \cdot (\varepsilon_r \mathbf{E}) = 0$. This corresponds to the case when the electric field is linearly polarized along one of the principal axes of $\vec{\varepsilon}_r$. Using the vector identity $\nabla \cdot (\psi \mathbf{A}) = \psi \nabla \cdot \mathbf{A} + (\nabla \psi) \cdot \mathbf{A}$, we have $\varepsilon_0 \nabla \cdot (\varepsilon_r \mathbf{E}) = \varepsilon_r \nabla \cdot \mathbf{E} + (\nabla \varepsilon_r) \cdot \mathbf{E} = 0$. In other words, in case of a scalar relative permittivity the right-hand side of the equation is $-\nabla \{ [(\nabla \varepsilon_r) / \varepsilon_r] \cdot \mathbf{E} \}$. Compared with the second term on the left-hand side, the right-hand side can be neglected when the relative change in ε_r over the distance of one wavelength must be much less than unity [37]. Finally, we obtain the following wave

$$\vec{\mathbf{R}}(\theta, \phi, \chi) = \begin{pmatrix} \cos(\theta)\cos(\phi)\cos(\chi) - \sin(\phi)\sin(\chi) & \cos(\theta)\cos(\chi)\sin(\phi) + \cos(\phi)\sin(\chi) & -\cos(\chi)\sin(\theta) \\ -\cos(\chi)\sin(\phi) - \cos(\theta)\cos(\phi)\sin(\chi) & \cos(\phi)\cos(\chi) - \cos(\theta)\sin(\phi)\sin(\chi) & \sin(\theta)\sin(\chi) \\ \cos(\phi)\sin(\theta) & \sin(\theta)\sin(\phi) & \cos(\theta) \end{pmatrix} \quad (\text{B2})$$

is an orthogonal rotation matrix parametrized by Euler angles as defined in Ref. [39]. In the rotating reference frame, it is convenient to choose a basis including the three principal axes of inertia. In this basis, the polarizability tensor has a simple representation,

$$\vec{\alpha}_{\text{mol}} = \begin{pmatrix} \alpha_{\perp} & 0 & 0 \\ 0 & \alpha_{\perp} & 0 \\ 0 & 0 & \alpha_{\parallel} \end{pmatrix}, \quad (\text{B3})$$

where $\alpha_{\parallel, \perp}$ are the polarizabilities along and perpendicular to the molecular axis, respectively.

equation [38]:

$$\nabla^2 \mathbf{E} - \mu_0 \varepsilon_0 \vec{\varepsilon}_r \frac{\partial^2 \mathbf{E}}{\partial t^2} = 0. \quad (\text{A9})$$

To further simplify Eq. (A9), we assume that the electric field propagates along the Z axis and substitute $\mathbf{E}(x, y, z, t) = \mathbf{U}(x, y, z) \exp[i(k_0 z - \omega t)]$. The chosen form of \mathbf{E} implies that we neglect the pulse nature of the light. Here $\mathbf{U}(x, y, z) = (U_x, U_y, 0)$ is the complex amplitude. For consistency with Sec. II, we use Hecht's phase convention [30], $k_0 z - \omega t$. The result reads

$$(\omega^2 \vec{\varepsilon}_r - c^2 k_0^2 \mathbf{I}) \mathbf{U} + c^2 \left(2ik_0 \frac{\partial \mathbf{U}}{\partial z} + \nabla^2 \mathbf{U} \right) = 0, \quad (\text{A10})$$

where $c = 1/\sqrt{\mu_0 \varepsilon_0}$, \mathbf{I} is the identity matrix, and \mathbf{e}_z is the unit vector along the Z axis. Next, we make the paraxial approximation and neglect the second derivative with respect to z , such that Eq. (A10) becomes

$$(\omega^2 \vec{\varepsilon}_r - c^2 k_0^2 \mathbf{I}) \mathbf{U} + c^2 \left(2ik_0 \frac{\partial \mathbf{U}}{\partial z} + \nabla_T^2 \mathbf{U} \right) = 0, \quad (\text{A11})$$

where ∇_T^2 is the transverse Laplacian operator. Rearrangement yields

$$\frac{\partial \mathbf{U}}{\partial z} = \frac{i}{2k_0} \nabla_T^2 \mathbf{U} + \frac{ik_0}{2} \left(\frac{\omega^2}{c^2 k_0^2} \vec{\varepsilon}_r - \mathbf{I} \right) \mathbf{U}.$$

Finally, we substitute $\omega^2/(c^2 k_0^2) = 1$, such that

$$\frac{\partial \mathbf{U}}{\partial z} = \frac{i}{2k_0} \nabla_T^2 \mathbf{U} + \frac{ik_0}{2} (\vec{\varepsilon}_r - \mathbf{I}) \mathbf{U}. \quad (\text{A12})$$

APPENDIX B: ROTATIONAL DYNAMICS

For free rigid linear molecules in the gas phase $(\vec{\alpha})_{\text{lab}}$ is simply a constant. In case of laser excited molecular gas, however $(\vec{\alpha})_{\text{lab}}$ is generally position dependent anisotropic tensor. The relation between the polarizability expressed in the molecule-fixed frame and the polarizability expressed in the laboratory-fixed frame,

$$\vec{\alpha}_{\text{lab}} = \vec{\mathbf{R}}^T \vec{\alpha}_{\text{mol}} \vec{\mathbf{R}}, \quad (\text{B1})$$

where

The explicit expression for $\langle \vec{\alpha} \rangle_{\text{lab}}$ in terms of the Euler angles reads

$$\langle \vec{\alpha} \rangle_{\text{lab}} = \begin{pmatrix} A & D & 0 \\ D & B & 0 \\ 0 & 0 & C \end{pmatrix}, \quad (\text{B4})$$

where

$$A = \frac{1}{4}[\alpha_{\parallel} + 3\alpha_{\perp} - \Delta\alpha \langle \cos(2\theta) - 2 \cos(2\phi) \sin^2(\theta) \rangle], \quad (\text{B5})$$

$$B = \frac{1}{4}[\alpha_{\parallel} + 3\alpha_{\perp} - \Delta\alpha \langle \cos(2\theta) + 2 \cos(2\phi) \sin^2(\theta) \rangle], \quad (\text{B6})$$

$$C = \frac{1}{2}[\alpha_{\parallel} + \alpha_{\perp} + \Delta\alpha \langle \cos(2\theta) \rangle], \quad (\text{B7})$$

$$D = \frac{\Delta\alpha}{2} \langle \sin(2\phi) \sin^2(\theta) \rangle, \quad (\text{B8})$$

with $\Delta\alpha = \alpha_{\parallel} - \alpha_{\perp}$.

Pump pulse(s) initiate rotational dynamics, such that, generally, the various expectation values appearing in Eqs. (B5), (B6), (B7), and (B8) depend on the probe delay. The evaluation of the elements of $\langle \vec{\alpha} \rangle_{\text{lab}}$ requires simulating the rotational dynamics of laser driven linear molecules. For the quantum mechanical simulations, we expressed the trigonometric functions involved in the matrix elements of $\langle \vec{\alpha} \rangle_{\text{lab}}$ in terms of Wigner D-functions as follows:

$$\cos(2\theta) - 2 \cos(2\phi) \sin^2(\theta) = \frac{4D_{00}^{2*} - 1}{3} - \sqrt{\frac{8}{3}}[D_{20}^{2*} + D_{-20}^{2*}], \quad (\text{B9})$$

$$\cos(2\theta) + 2 \cos(2\phi) \sin^2(\theta) = \frac{4D_{00}^{2*} - 1}{3} + \sqrt{\frac{8}{3}}[D_{20}^{2*} + D_{-20}^{2*}], \quad (\text{B10})$$

$$\cos(2\theta) = \frac{4D_{00}^{2*} - 1}{3}, \quad (\text{B11})$$

$$\frac{1}{2} \sin(2\phi) \sin^2(\theta) = i\sqrt{\frac{1}{6}}[D_{-20}^{2*} - D_{20}^{2*}]. \quad (\text{B12})$$

-
- [1] H. Stapelfeldt and T. Seideman, Colloquium: Aligning molecules with strong laser pulses, *Rev. Mod. Phys.* **75**, 543 (2003).
- [2] S. Fleischer, Y. Khodorkovsky, E. Gershnel, Y. Prior, and I. Sh. Averbukh, Molecular alignment induced by ultrashort laser pulses and its impact on molecular motion, *Isr. J. Chem.* **52**, 414 (2012).
- [3] M. Lemeshko, R. V. Krems, J. M. Doyle, and S. Kais, Manipulation of molecules with electromagnetic fields, *Mol. Phys.* **111**, 1648 (2013).
- [4] C. P. Koch, M. Lemeshko, and D. Sugny, Quantum control of molecular rotation, *Rev. Mod. Phys.* **91**, 035005 (2019).
- [5] D. Normand, L. A. Lompre, and C. Cornaggia, Laser-induced molecular alignment probed by a double-pulse experiment, *J. Phys. B: At., Mol. Opt. Phys.* **25**, L497 (1992).
- [6] P. Dietrich, D. T. Strickland, M. Laberge, and P. B. Corkum, Molecular reorientation during dissociative multiphoton ionization, *Phys. Rev. A* **47**, 2305 (1993).
- [7] A. T. J. B. Eppink and D. H. Parker, Velocity map imaging of ions and electrons using electrostatic lenses: Application in photoelectron and photofragment ion imaging of molecular oxygen, *Rev. Sci. Instrum.* **68**, 3477 (1997).
- [8] E. T. Karamatskos, S. Raabe, T. Mullins, A. Trabattori, P. Stammer, G. Goldsztejn, R. R. Johansen, K. Długołeccki, H. Stapelfeldt, M. J. J. Vrakking, S. Trippel, A. Rouzée, and J. Küpper, Molecular movie of ultrafast coherent rotational dynamics of OCS, *Nat. Commun.* **10**, 3364 (2019).
- [9] R. Dörner, V. Mergel, O. Jagutzki, L. Spielberger, J. Ullrich, R. Moshammer, and H. Schmidt-Böcking, Cold target recoil ion momentum spectroscopy: A “momentum microscope” to view atomic collision dynamics, *Phys. Rep.* **330**, 95 (2000).
- [10] K. Mizuse, K. Kitano, H. Hasegawa, and Y. Ohshima, Quantum unidirectional rotation directly imaged with molecules, *Sci. Adv.* **1**, e1400185 (2015).
- [11] K. Lin, Q. Song, X. Gong, Q. Ji, H. Pan, J. Ding, H. Zeng, and J. Wu, Visualizing molecular unidirectional rotation, *Phys. Rev. A* **92**, 013410 (2015).
- [12] K. Lin, I. Tutunnikov, J. Qiang, J. Ma, Q. Song, Q. Ji, W. Zhang, H. Li, F. Sun, X. Gong, H. Li, P. Lu, H. Zeng, Y. Prior, I. Sh. Averbukh, and J. Wu, All-optical field-free three-dimensional orientation of asymmetric-top molecules, *Nat. Commun.* **9**, 5134 (2018).
- [13] O. Faucher, B. Lavorel, E. Hertz, and F. Chaussard, Optically probed laser-induced field-free molecular alignment, in *Progress in Ultrafast Intense Laser Science VII*, edited by K. Yamanouchi, D. Charalambidis, and D. Normand (Springer, Berlin, 2011), pp. 79–108.

- [14] S. Fleischer, Y. Zhou, R. W. Field, and K. A. Nelson, Molecular Orientation and Alignment by Intense Single-Cycle THz Pulses, *Phys. Rev. Lett.* **107**, 163603 (2011).
- [15] R. Damari, S. Kallush, and S. Fleischer, Rotational Control of Asymmetric Molecules: Dipole-Versus Polarizability-Driven Rotational Dynamics, *Phys. Rev. Lett.* **117**, 103001 (2016).
- [16] V. Renard, M. Renard, S. Guérin, Y. T. Pashayan, B. Lavorel, O. Faucher, and H. R. Jauslin, Postpulse Molecular Alignment Measured by a Weak Field Polarization Technique, *Phys. Rev. Lett.* **90**, 153601 (2003).
- [17] S. J. Weber, M. Oppermann, and J. P. Marangos, Role of Rotational Wave Packets in Strong Field Experiments, *Phys. Rev. Lett.* **111**, 263601 (2013).
- [18] G. Karras, E. Hertz, F. Billard, B. Lavorel, G. Siour, J.-M. Hartmann, O. Faucher, E. Gershnel, Y. Prior, and I. Sh. Averbukh, Experimental observation of fractional echoes, *Phys. Rev. A* **94**, 033404 (2016).
- [19] Y. He, L. He, P. Lan, B. Wang, L. Li, X. Zhu, W. Cao, and P. Lu, Direct imaging of molecular rotation with high-order-harmonic generation, *Phys. Rev. A* **99**, 053419 (2019).
- [20] J. Bert, E. Prost, I. Tutunnikov, P. Béjot, E. Hertz, F. Billard, B. Lavorel, U. Steinitz, I. Sh. Averbukh, and O. Faucher, Optical imaging of coherent molecular rotors, *Laser Photon. Rev.* **14**, 1900344 (2020).
- [21] I. Sh. Averbukh and N. F. Perelman, Fractional revivals: Universality in the long-term evolution of quantum wave packets beyond the correspondence principle dynamics, *Phys. Lett. A* **139**, 449 (1989).
- [22] R. Robinett, Quantum wave packet revivals, *Phys. Rep.* **392**, 1 (2004).
- [23] K. Moh, X.-C. Yuan, J. Bu, R. Burge, and B. Z. Gao, Generating radial or azimuthal polarization by axial sampling of circularly polarized vortex beams, *Appl. Opt.* **46**, 7544 (2007).
- [24] B. Lei and S. Liu, Efficient polarization direction measurement by utilizing the polarization axis finder and digital image processing, *Opt. Lett.* **43**, 2969 (2018).
- [25] R. Yamaguchi, T. Nose, and S. Sato, Liquid crystal polarizers with axially symmetrical properties, *Jpn. J. Appl. Phys.* **28**, 1730 (1989).
- [26] M. Stalder and M. Schadt, Linearly polarized light with axial symmetry generated by liquid-crystal polarization converters, *Opt. Lett.* **21**, 1948 (1996).
- [27] Y. Kozawa and S. Sato, Generation of a radially polarized laser beam by use of a conical Brewster prism, *Opt. Lett.* **30**, 3063 (2005).
- [28] M. Erdélyi and G. Gajdáty, Radial and azimuthal polarizer by means of a birefringent plate, *J. Optics A: Pure Appl. Optics* **10**, 055007 (2008).
- [29] I. Moreno, J. Albero, J. A. Davis, D. M. Cottrell, and J. B. Cushing, Polarization manipulation of radially polarized beams, *Opt. Eng.* **51**, 128003 (2012).
- [30] E. Hecht, *Optics*, 5th ed. (Pearson, London, UK, 2016).
- [31] I. Tutunnikov, J. Floß, E. Gershnel, P. Brumer, and I. Sh. Averbukh, Laser-induced persistent orientation of chiral molecules, *Phys. Rev. A* **100**, 043406 (2019).
- [32] G. Karras, M. Ndong, E. Hertz, D. Sugny, F. Billard, B. Lavorel, and O. Faucher, Polarization Shaping for Unidirectional Rotational Motion of Molecules, *Phys. Rev. Lett.* **114**, 103001 (2015).
- [33] S. Fleischer, Y. Khodorkovsky, Y. Prior, and I. Sh. Averbukh, Controlling the sense of molecular rotation, *New J. Phys.* **11**, 105039 (2009).
- [34] U. Steinitz, Y. Prior, and I. Sh. Averbukh, Optics of a Gas of Coherently Spinning Molecules, *Phys. Rev. Lett.* **112**, 013004 (2014).
- [35] V. Renard, O. Faucher, and B. Lavorel, Measurement of laser-induced alignment of molecules by cross defocusing, *Opt. Lett.* **30**, 70 (2005).
- [36] A. Korobenko, A. A. Milner, and V. Milner, Direct Observation, Study, and Control of Molecular Superrotors, *Phys. Rev. Lett.* **112**, 113004 (2014).
- [37] D. Marcuse, *Light Transmission Optics* (Krieger, Malabar, FL, 1989).
- [38] L. W. Casperson, Gaussian light beams in inhomogeneous media, *Appl. Opt.* **12**, 2434 (1973).
- [39] R. Zare, *Angular Momentum: Understanding Spatial Aspects in Chemistry and Physics* (Wiley, New York, 1988).